Mechanical Systems and Signal Processing 224 (2025) 111991

Contents lists available at ScienceDirect

Mechanical Systems and Signal Processing

journal homepage: www.elsevier.com/locate/ymssp

Unbalance compensation based on speed fault-tolerance and fusion strategy for magnetically suspended PMSM☆

Runhui Yao, Yuanping Xu *, Renkun Zhang, Yue Zhang, Jin Zhou *

Department of Mechanical and Electrical Engineering, Nanjing University of Aeronautics and Astronautics, Nanjing 210016, China

ARTICLE INFO

Communicated by Jose Rodellar

Keywords:
Active magnetic bearing
Unbalance compensation
Speed estimation
Fault-tolerance
Information fusion

ABSTRACT

High-reliability rotor speed estimation method is essential for implementing unbalance compensation of magnetically suspended permanent magnet synchronous motors (PMSM) without speed sensors. However, the current investigations rarely focus on the fault-tolerance of speed estimation methods, making it challenging to achieve stable and reliable operation of magnetically suspended PMSM upon the impacts represented by DC offset and shock excitation. Herein, a novel speed fault-tolerance and fusion strategy (SFTFS) is proposed to improve the reliability and accuracy of rotor speed estimation. Making use of this strategy which involves in the acquisition of two independent yet redundant speed information from the vibration displacement of rotor and sensorless vector control systems of PMSM, it is feasible to realize automatic diagnosis and isolation of abnormal speed information using the innovation noise characteristics of local Kalman filters when one speed estimation method fails, thus ensuring the validity of speed information. Moreover, when both speed estimation methods are functioning normally, the strategy solves for the optimal fusion matrix weights based on the noise characteristics of two speed information, thereby adaptively optimizing the fusion and enhancing the accuracy of speed information. Finally, the proposed strategy was experimentally validated on a magnetically suspended turbo molecular pump, highlighting its effectiveness and superiority.

1. Introduction

Featured with the distinguished merits including high power density, fine-tuning speed, lubrication-free, and long durability, magnetically suspended permanent magnet synchronous motors (PMSM) have been widely used in high-speed rotating machinery domains [1–3] such as control moment gyros [4,5], turbo molecular pumps [6,7] and flywheel energy storage system [8,9]. However, the unbalanced vibration of rotor initiated from its inevitable residual mass unbalance, has long been a critical issue to deteriorate the operational performance and stability of magnetically suspended PMSM [10].

To suppress the unbalanced vibration of rotor, the general approach is to adopt the active control characteristics of magnetic bearings (AMB) [11]. Specifically, considering that magnetically suspended PMSM typically operates at high speeds, unbalance compensation is often employed to reduce the risk of actuator saturation and increase the speed limit of rotor. The key of unbalance compensation lies in the accurate extraction of synchronous component from the rotor vibration displacement, which usually requires precise speed information provided by speed sensors [12]. Unfortunately, it should be signified that the application of speed sensors in

☆ This work was supported in part by the National Natural Science Foundation of China under Grant 52475060 and 52075239.
* Corresponding authors.
E-mail addresses: ypxu@nuaa.edu.cn (Y. Xu), zhj@nuaa.edu.cn (J. Zhou).

https://doi.org/10.1016/j.ymssp.2024.111991
Received 8 July 2024; Received in revised form 7 September 2024; Accepted 25 September 2024
Available online 1 October 2024

Nomenclature

$\omega,\omega_0,\omega_e\omega_{0,v},\omega_{0,e},\omega_{0,f}$	Rotor speed, notch angular frequency, electrical speed, speed estimated by second-order generalized integrators-frequency-locked loop (SOGI-FLL), speed estimated by full-order sliding mode observer-phase-locked loop (FSMO-PLL), fused speed
$\theta,\theta_e,\theta_{0,e}$	Rotor position, electrical rotor position, position estimated by FSMO-PLL
v_α,v_β	Synchronous output and orthogonal output of SOGI-FLL
γ	Frequency estimation gain of FLL
$u_\alpha,u_\beta,i_\alpha,i_\beta$	PMSM voltage and current in static-coordinate
E_α,E_β	PMSM back electromotive force in static-coordinate
R_s,L_s,ψ_m,P_n	Stator resistance, inductance, rotor flux and pole pairs of PMSM
k_i,k_e	Current and back electromotive force sliding mode gains of FSMO
T_s	Sampling time
$\boldsymbol{x}_i,\boldsymbol{z}_i$	State and measurement of the ith local Kalman filter (KF)
$\hat{\boldsymbol{x}}_i^-,\hat{\boldsymbol{x}}_i$	Priori state estimation and posteriori state estimation of the ith local KF
$\hat{\boldsymbol{x}}_f,\boldsymbol{P}_f$	Optimal fusion state estimation and optimal fusion state estimation error covariance
$\boldsymbol{P}_i,\boldsymbol{P}_i^-$	Local state estimation error covariance and priori state estimation error covariance of the ith local KF
$P_{\omega i},P_{\omega f}$	Speed estimation error variance of the ith local KF and optimal fusion state estimation
$\boldsymbol{P}$	Composite error covariance
$\boldsymbol{A},\boldsymbol{w}$	State transition and process noise
$\boldsymbol{Q}$	Process noise covariance
$\boldsymbol{H}_i,\boldsymbol{v}_i$	Measurement transition and measurement noise of the ith local KF
$\boldsymbol{R}_i,\boldsymbol{r}_i$	Measurement noise covariance and measurement noise offset of the ith local KF
$\boldsymbol{K}_i,\boldsymbol{I}_i$	Kalman gain and innovation of the ith local KF
λ_t,λ_i	Fault detection threshold and test statistics of the ith local KF
$\boldsymbol{\Lambda}_i$	Optimal fusion matrix weights of the ith local KF

magnetically suspended PMSM would be strictly restrained in scenarios requiring high durability, cost-efficiency, compact size or harsh working conditions [13].

In this regard, unbalance compensation based on rotor speed estimation has emerged as an alternative approach. Up to date, plenty of unbalance compensation methods with speed estimation based on adaptive notch filters [14–16], second-order generalized integrators-frequency-locked loops (SOGI-FLL) [12,17–19] and orthogonal phase-locked loops (PLL) [20,21], have been proposed and demonstrated to be effective. Despite the above-mentioned methods have made significant and continues progress in unbalance compensation, its reliability in cases wherein input signal contains unrelated noise, i.e., DC offset and shock excitation [22–25], remains to be a challenge, posing a burden for broadening its applications. More importantly, it is noteworthy that the current investigations rarely focus on the speed fault-tolerance capacity of unbalance compensation, suggesting the high potential risk of unbalance compensation error and consequently failure. The exploration of highly-reliable unbalance compensation with speed fault-tolerance capacity is still an ongoing task.

Recently, motivated by the sensorless control of PMSM, an innovative speed redundant unbalance compensation was proposed by Hutterer [26]. Different from conventional unbalance compensation that solely rely on speed information from rotor vibration displacement, redundant speed information was also obtained using the electrical signals such as current and voltage in the sensorless vector control system of PMSM. By utilizing the two independent speed information, it is possible to switch to the alternative speed information when one fails, permitting the speed redundant capability of unbalance compensation. Hutterer presented a new perspective to enhance the reliability of speed estimation for magnetically suspended PMSM. Nevertheless, this approach still suffers from some limitations more or less. First, it necessitates manual switching when the speed information from rotor vibration displacement fails or presents declined precision, which would increase the operational complexity. Second, the direct switching between two speed information may introduce erroneous speed information, potentially resulting in the failure of unbalance compensation. Thus, to enable the high reliability and adaptability of unbalance compensation, further work is required to endow it with automatic fault diagnosis and isolation capability for speed estimation.

Herein, in this work, a speed fault-tolerance and fusion strategy (SFTFS) for unbalance compensation of magnetically suspended PMSM is proposed by adopting the principle and characteristics of federated Kalman filter. The federated Kalman filter, which can achieve real-time information fusion and facilitate fault diagnosis and isolation due to the inherent distributed structure, has been widely applied in fields such as multi-sensor fusion [27,28] and integrated navigation [29–31]. From the theoretical aspect, one can also employ the aforementioned characteristics of federated Kalman filter to perform the fault-tolerance and fusion of the two independent speed information from rotor vibration displacement and electrical signals. Specifically, one can utilize the noise characteristics of innovation in local Kalman filters to automatically diagnosis and isolate anomalous speed information, ensuring the validity of speed information. In the cases where two speed estimation methods are functioning properly, it can use the noise characteristics of each speed information to solve optimal fusion matrix weights. As a consequence, real-time adaptive optimal fusion of the two independent speed information can be realized and enhancing the accuracy of speed estimation. The fused speed information can

be subsequently applied in unbalance compensation to achieve high-reliability.

The main contributions of this paper can be summarized as follows:

1) A speed fault-tolerance and fusion strategy for unbalance compensation of magnetically suspended PMSM is proposed on the basis of obtaining two independent yet redundant speed information from the vibration displacement of rotor and sensorless vector control systems of PMSM. The strategy enables automatic fault diagnosis and isolation of anomalous speed information, guaranteeing the validity of speed information and enhancing the reliability of unbalance compensation for magnetically suspended PMSM.
2) When the speed estimation methods based on rotor vibration displacement and electrical signals are functioning properly, the proposed strategy enables real-time adaptive optimal fusion of speed information, reducing the noise level of fused speed information and enhancing the accuracy of speed estimation.
3) The proposed strategy was applied to the control system of a magnetically suspended turbo molecular pump, demonstrating its feasibility and superiority in unbalance compensation.

2. Brief working principle of unbalance compensation for AMB

The unbalance compensation for AMB commonly adopts generalized notch filter, which can extract and filter out the synchronous component from the rotor vibration displacement. As a result, the AMB would only control the position of mass center of rotor. The schematic diagram of the unbalance compensation for AMB is shown in Fig. 1.

The transfer function $N(s)$ of the notch filter is:

$$N(s) = \frac{s^2 + \omega_0^2}{s^2 + \xi\omega_0 s + \omega_0^2}, N(\mathrm{j}\omega) = \begin{cases} 1, \omega \neq \omega_0 \\ 0, \omega = \omega_0 \end{cases} \tag{1}$$

where the notch angular frequency ω_0 should follow the variation of rotor speed to ensure the effectiveness of the unbalance compensation within the whole speed range. When the speed sensor is unavailable, a speed estimation method is required to obtain ω_0. In the magnetically suspended PMSM, there are two ways to obtain ω_0 without speed sensors. One way is to estimate speed by the vibration displacement of rotor. Another way is to estimate speed by using the electrical signals such as current and voltage of PMSM.

3. Speed estimation methods for magnetically suspended PMSM

Magnetically suspended PMSM generally rely on direct-drive structure. The control system of AMB and PMSM can control the same rotor based on vibration displacement and electrical signals, respectively. This allows the two control systems to obtain speed information in independent manners. The following section will illustrate the two independent speed estimation methods based on AMB and PMSM, respectively.

3.1. Speed estimation method of AMB

Due to the low stiffness of AMB and mass unbalance of rotor, unbalanced vibration of rotor would be induced and it possesses the same frequency with rotor speed. SOGI-FLL is a single-phase synchronous system that can estimate rotor speed based on the vibration displacement of rotor and its overall structure is manifested in Fig. 2 [19].

From Fig. 2, it can be seen that the transfer functions from the input signal v to the error signal e and the orthogonal output of SOGI v_β are:

$$\frac{e(s)}{v(s)} = \frac{s^2 + \omega_{0,\mathrm{v}}^2}{s^2 + k_\mathrm{v}\omega_{0,\mathrm{v}} s + \omega_{0,\mathrm{v}}^2} \tag{2}$$

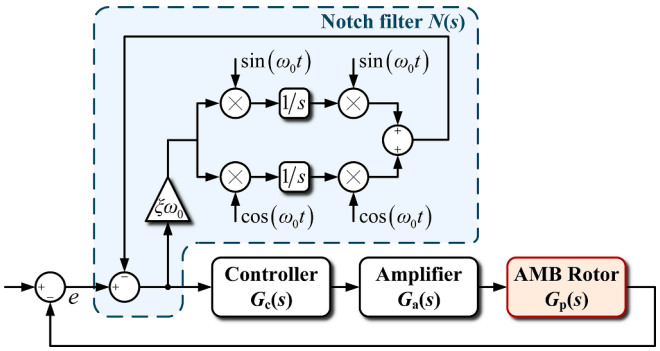

Fig. 1. Schematic diagram of the brief working principle of unbalance compensation for AMB.

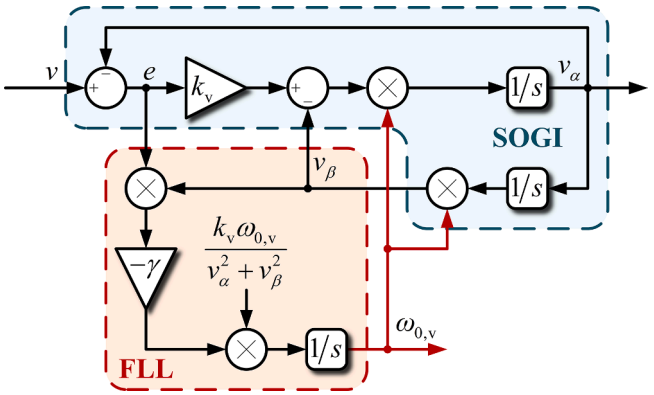

Fig. 2. Structure diagram of SOGI-FLL.

$$\frac{v_\beta(s)}{v(s)}=\frac{k_v\omega_{0,v}^2}{s^2+k_v\omega_{0,v}s+\omega_{0,v}^2} \tag{3}$$

The frequency estimation equation of FLL is:

$$\frac{d\omega_{0,v}}{dt}=\frac{-\gamma k_v\omega_{0,v}}{v_\alpha^2+v_\beta^2}(ev_\beta) \tag{4}$$

According to Eq. (2) and Eq. (3), it can be concluded that when the angular frequency of $\omega_{0,v}$ is greater than that of v, e will be in phase with v_β, and $\omega_{0,v}$ will decrease under the influence of the frequency estimation equation. When the angular frequency of $\omega_{0,v}$ is smaller than that of v, the phase of e and v_β will be opposite, and $\omega_{0,v}$ will increase under the influence of the frequency estimation equation. Finally, $\omega_{0,v}$ will converge to the angular frequency of v. Thus, the speed information $\omega_{0,v}$ can be obtained from the vibration displacement of rotor, which serves as the basis for SFTFS.

3.2. Speed estimation method of PMSM

The sensorless vector control method for PMSM is mature. Considering the control accuracy and computational requirements of the system, full-order sliding mode observer-phase-locked loop (FSMO-PLL) is adopted here for sensorless control of PMSM [32]. The necessary rotor speed and angle information in sensorless vector control will be adopted as the basis for the SFTFS proposed in this work.

The rotor of magnetically suspended PMSM with direct-drive structure usually in the form of surface mounted permanent magnets, and the voltage equation of PMSM in static-coordinate is:

$$\begin{bmatrix}u_\alpha\\u_\beta\end{bmatrix}=R_s\begin{bmatrix}i_\alpha\\i_\beta\end{bmatrix}+L_s\frac{d}{dt}\begin{bmatrix}i_\alpha\\i_\beta\end{bmatrix}+\begin{bmatrix}E_\alpha\\E_\beta\end{bmatrix} \tag{5}$$

where E_α and E_β are the components of back electromotive force (Back EMF) in static-coordinate, and their expressions are:

$$\begin{bmatrix}E_\alpha\\E_\beta\end{bmatrix}=\psi_m\omega_e\begin{bmatrix}-\sin\theta_e\\\cos\theta_e\end{bmatrix} \tag{6}$$

According to Eq. (6), one can see that the back electromotive force is related to the electrical position. Due to the inability to directly measure the back electromotive force, it is necessary to reconstruct it with FSMO. The expression for FSMO is:

$$\frac{d}{dt}\begin{bmatrix}\hat{\boldsymbol{i}}_s\\\hat{\boldsymbol{E}}_s\end{bmatrix}=\begin{bmatrix}\boldsymbol{M}_{11}&\boldsymbol{M}_{12}\\\boldsymbol{0}&\hat{\boldsymbol{\omega}}\end{bmatrix}\begin{bmatrix}\hat{\boldsymbol{i}}_s\\\hat{\boldsymbol{E}}_s\end{bmatrix}-\begin{bmatrix}\boldsymbol{M}_{12}\\\boldsymbol{0}\end{bmatrix}\boldsymbol{u}_s-\frac{1}{L_s}\boldsymbol{K}\mathrm{sgn}(\hat{\boldsymbol{i}}_s-\boldsymbol{i}_s) \tag{7}$$

where:

$$\hat{\boldsymbol{i}}_s=\begin{bmatrix}\hat{i}_\alpha\\\hat{i}_\beta\end{bmatrix};\boldsymbol{i}_s=\begin{bmatrix}i_\alpha\\i_\beta\end{bmatrix};\hat{\boldsymbol{E}}_s=\begin{bmatrix}\hat{E}_\alpha\\\hat{E}_\beta\end{bmatrix};\boldsymbol{M}_{11}=\begin{bmatrix}-R_s/L_s&0\\0&-R_s/L_s\end{bmatrix};\boldsymbol{M}_{12}=\begin{bmatrix}-1/L_s&0\\0&-1/L_s\end{bmatrix};\hat{\boldsymbol{\omega}}=\begin{bmatrix}0&-\hat{\omega}_e\\\hat{\omega}_e&0\end{bmatrix};\boldsymbol{u}_s=\begin{bmatrix}u_\alpha\\u_\beta\end{bmatrix};\boldsymbol{K}=\begin{bmatrix}k_i&0&-k_e&0\\0&k_i&0&-k_e\end{bmatrix}^T$$

When k_i and k_e satisfy $k_i>\max(|E_\alpha-\hat{E}_\alpha|,|E_\beta-\hat{E}_\beta|)$ and $k_e>0$, the FSMO converges asymptotically, and increasing k_e/k_i can improve the convergence speed of the back electromotive force. Given that the stability of FSMO has been proven in [33,34], this paper will not elaborate it further. After obtaining the back electromotive force, the electrical position information can be extracted through

a PLL, and the electrical speed can be obtained through differentiation of electrical position. The structure diagram of PLL is given in Fig. 3:

The input of the PI regulator of PLL is:

$$\left(-\widehat{E}_{\alpha}\cos\widehat{\theta}_{\mathrm{e}}-\widehat{E}_{\beta}\sin\widehat{\theta}_{\mathrm{e}}\right)/\sqrt{\widehat{E}_{\alpha}^{2}+\widehat{E}_{\beta}^{2}}=\sin(\theta_{\mathrm{e}}-\widehat{\theta}_{\mathrm{e}}) \tag{8}$$

When $\theta_{\mathrm{e}}-\widehat{\theta}_{\mathrm{e}}$ is smaller than $\pi/6$, $\sin(\theta_{\mathrm{e}}-\widehat{\theta}_{\mathrm{e}})$ can be approximated to $\theta_{\mathrm{e}}-\widehat{\theta}_{\mathrm{e}}$. By using PI regulator, the error of closed-loop system $\theta_{\mathrm{e}}-\widehat{\theta}_{\mathrm{e}}$ can approach 0, that is, $\widehat{\theta}_{\mathrm{e}}$ will approach θ_{e}, and the output of the PI regulator is $\widehat{\omega}_{\mathrm{e}}$. After dividing the obtained $\widehat{\omega}_{\mathrm{e}}$ and $\widehat{\theta}_{\mathrm{e}}$ by the pole pairs P_{n} of PMSM, we can obtain the rotor speed $\omega_{0,\mathrm{e}}$ and position $\theta_{0,\mathrm{e}}$. The block diagram of the speed and angle estimation method based on FSMO-PLL is presented in Fig. 4:

4. Speed fault-tolerance and fusion strategy

Once obtaining the two independent speed information from AMB and PMSM, then speed fault-tolerance and fusion strategy can be applied. When any speed estimation method fails, the system will automatically diagnose the fault and isolate the abnormal speed information to ensure the validity of speed information required for unbalance compensation; When both speed estimation methods are working properly, the two independent speed information can be adaptively fused according to their noise characteristics. As a result, the fused speed information is capable of remaining a lower noise level.

Considering that the federated Kalman filter can achieve real-time information fusion and its distributed structure is of great benefit to facilitate real-time fault diagnosis and isolation, the SFTFS for magnetically suspended PMSM is proposed based on the principle and characteristics of federated Kalman filter. The brief working principle of SFTFS is shown in Fig. 5, which mainly includes three parts: adaptive local Kalman filter, fault diagnosis and isolation module, and matrix weighted optimal fusion module.

4.1. Adaptive local Kalman filter

The local Kalman filter can adaptively adjust the measurement noise covariance and the Kalman gain according to the noise characteristics of the speed information, and output the real-time local state estimation as well as the local state estimation error covariance for matrix weighted optimal fusion. The local Kalman filter KF1 is designed for tracking $\omega_{0,\mathrm{v}}$ and the local Kalman filter KF2 is designed for tracking $\theta_{0,\mathrm{e}}$ and $\omega_{0,\mathrm{e}}$.

The magnetically suspended PMSM often operates at rated speed, and the rate is low during acceleration and deceleration. The rotor speed can be approximately unchanged in the adjacent two control cycles. Therefore, based on the dynamic equation of the rotational freedom, a state update equation with process noise can be constructed as follows:

$$\boldsymbol{x}_{[k+1]}=\boldsymbol{A}\boldsymbol{x}_{[k]}+\boldsymbol{w}_{[k]} \tag{9}$$

where:

$$\boldsymbol{x}=\begin{bmatrix}\theta\\ \omega\end{bmatrix};\boldsymbol{A}=\begin{bmatrix}1 & T_{\mathrm{s}}\\ 0 & 1\end{bmatrix};\boldsymbol{w}\sim\mathrm{N}(\boldsymbol{0},\boldsymbol{Q})$$

As Eq. (9) does not include control variables and $\boldsymbol{A}$ does not change over time, $\boldsymbol{Q}$ can be regarded as a steady matrix [35].

Based on the analysis in section 3, it can be concluded that according to the vibration displacement of rotor, SOGI-FLL can only provide speed information $\omega_{0,\mathrm{v}}$, while in the sensorless vector control system of PMSM, FSMO-PLL can provide both speed information $\omega_{0,\mathrm{e}}$ and position information $\theta_{0,\mathrm{e}}$. The measurement equations for KF1 and KF2 are constructed as follows:

$$\boldsymbol{z}_{i[k]}=\boldsymbol{H}_{i}\boldsymbol{x}_{[k]}+\boldsymbol{v}_{i[k]},i=1,2 \tag{10}$$

where:

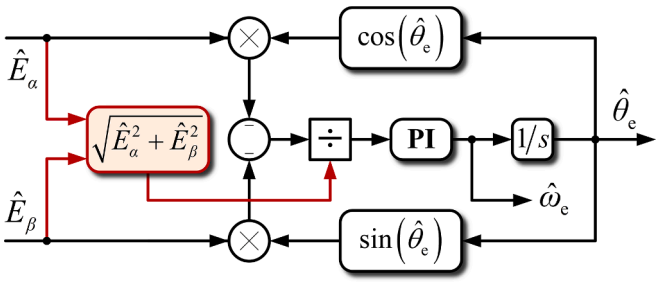

Fig. 3. Structure diagram of PLL.

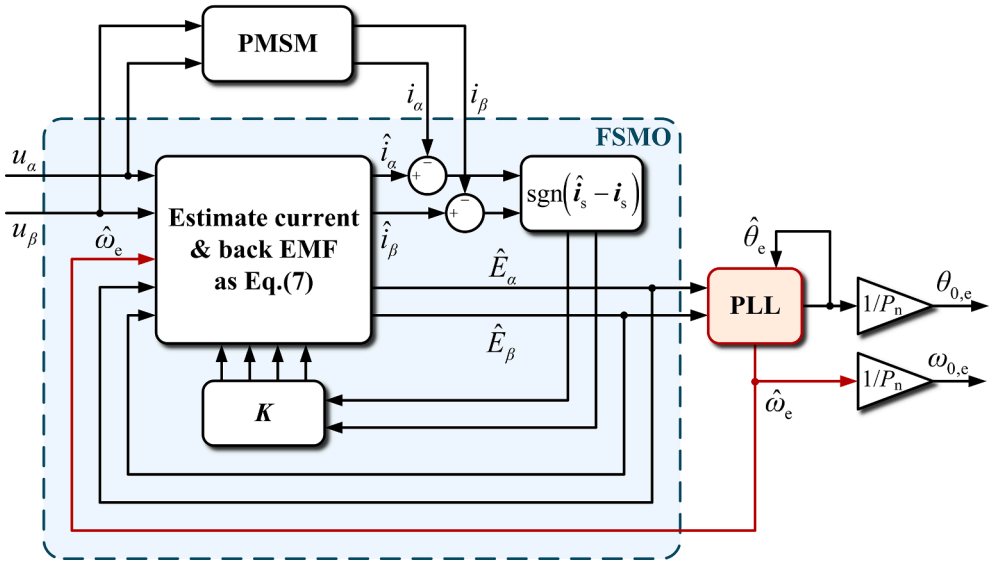

Fig. 4. Block diagram of the speed and angle estimation method based on FSMO-PLL.

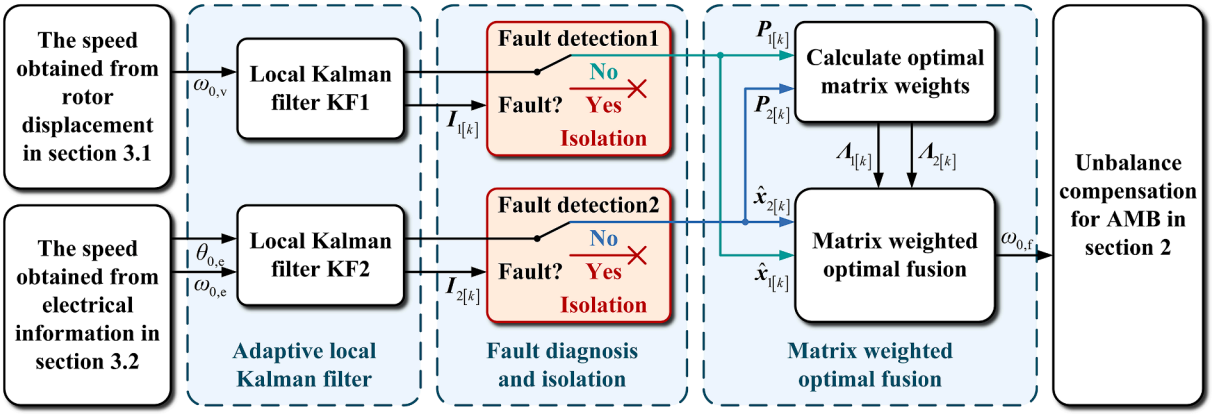

Fig. 5. The brief working principle of SFTFS.

$$\boldsymbol{z}_1 = \omega_{0,\mathrm{v}}; \boldsymbol{z}_2 = \begin{bmatrix} \theta_{0,\mathrm{e}} \\ \omega_{0,\mathrm{e}} \end{bmatrix}; \boldsymbol{H}_1 = [\,0 \quad 1\,]; \boldsymbol{H}_2 = \begin{bmatrix} 1 & 0 \\ 0 & 1 \end{bmatrix}; \boldsymbol{\nu}_1 \sim \mathrm{N}(0, R_1); \boldsymbol{\nu}_2 \sim \mathrm{N}(\boldsymbol{0}, \boldsymbol{R}_2)$$

During the operation of magnetically suspended PMSM, the noises and disturbances in the control system can cause the oscillation of $\omega_{0,\mathrm{v}}$, $\omega_{0,\mathrm{e}}$, and $\theta_{0,\mathrm{e}}$ near the true speed ω and the true angle θ. Thus, the measurement noise $\boldsymbol{\nu}$ in the local Kalman filter is time-varying, and its covariance $\boldsymbol{R}$ is also time-varying. Given that the relationship between $\boldsymbol{R}$ and $\boldsymbol{Q}$ will determine the performance of the local Kalman filter [36], this paper chooses the Sage-Husa adaptive method for real-time tuning of $\boldsymbol{R}$. The iterative process of adaptive local Kalman filter KFi; $i = 1,2$ is described as follows:

1) Calculate the priori state estimation and priori state estimation error covariance based on the previous step's local state estimation and the local state estimation error covariance:

$$\hat{\boldsymbol{x}}^{-}_{i[k+1]} = \boldsymbol{A}\hat{\boldsymbol{x}}_{i[k]} \tag{11}$$

$$\boldsymbol{P}^{-}_{i[k+1]} = \boldsymbol{A}\boldsymbol{P}_{i[k]}\boldsymbol{A}^{\mathrm{T}} + \boldsymbol{Q} \tag{12}$$

2) Introduce the measurement and solve the measurement noise covariance using time averaging method:

$$d_k = (1-b)/\left(1-b^{k+1}\right) \tag{13}$$

$$\boldsymbol{r}_{i[k+1]} = (1-d_k)\boldsymbol{r}_{i[k]} + d_k\left(\boldsymbol{z}_{i[k+1]} - \boldsymbol{H}_i\widehat{\boldsymbol{x}}^-_{i[k+1]}\right) \tag{14}$$

$$\boldsymbol{\varepsilon}_{i[k+1]} = \boldsymbol{z}_{i[k+1]} - \boldsymbol{H}_i\widehat{\boldsymbol{x}}^-_{i[k+1]} - \boldsymbol{r}_{i[k+1]} \tag{15}$$

$$\boldsymbol{R}_{i[k+1]} = (1-d_k)\boldsymbol{R}_{i[k]} + d_k\left(\boldsymbol{\varepsilon}_{i[k+1]}\boldsymbol{\varepsilon}^{\mathrm{T}}_{i[k+1]} - \boldsymbol{H}_i\boldsymbol{P}^-_{i[k+1]}\boldsymbol{H}_i^{\mathrm{T}}\right) \tag{16}$$

3) Calculate the Kalman gain based on the priori state estimation error covariance and measurement noise covariance, and then fuse the priori state estimation with the measurement to obtain the local state estimation and the local state estimation error covariance:

$$\boldsymbol{K}_{i[k+1]} = \boldsymbol{P}^-_{i[k+1]}\boldsymbol{H}_i^{\mathrm{T}}\left(\boldsymbol{H}_i\boldsymbol{P}^-_{i[k+1]}\boldsymbol{H}_i^{\mathrm{T}} + \boldsymbol{R}_{i[k+1]}\right) \tag{17}$$

$$\widehat{\boldsymbol{x}}_{i[k+1]} = \widehat{\boldsymbol{x}}^-_{i[k+1]} + \boldsymbol{K}_{i[k+1]}\boldsymbol{\varepsilon}_{i[k+1]} \tag{18}$$

$$\boldsymbol{P}_{i[k+1]} = \boldsymbol{P}^-_{i[k+1]} - \boldsymbol{K}_{i[k+1]}\boldsymbol{H}_i\boldsymbol{P}^-_{i[k+1]} \tag{19}$$

where, b is the forgetting factor, which is usually taken as 0.95 ~ 0.99 [37]. In this paper, b is set to be 0.99. Fig. 6 presents the schematic diagram of the iterative process of the adaptive local Kalman filter.

4.2. Fault diagnosis and isolation

During the normal operation of magnetically suspended PMSM, the state of the two adjacent time steps should satisfy Eq. (9). If the speed estimation method is proper at and before the kth time step, then $\widehat{\boldsymbol{x}}_{i[k]}$ represents the local state estimation at the kth time step. Then, the predicted value of the measurement can be obtained based on the state transition and measurement transition:

$$\widehat{\boldsymbol{z}}^-_{i[k+1]} = \boldsymbol{H}_i\boldsymbol{A}\widehat{\boldsymbol{x}}_{i[k]} \tag{20}$$

The difference between $\boldsymbol{z}_{i[k+1]}$ and $\widehat{\boldsymbol{z}}^-_{i[k+1]}$ is the innovation $\boldsymbol{I}$, which is usually manifested in the form of white noise, and its covariance is:

$$\mathrm{E}\left(\boldsymbol{I}_{i[k+1]}\boldsymbol{I}^{\mathrm{T}}_{i[k+1]}\right) = \boldsymbol{H}_i\boldsymbol{P}^-_{i[k+1]}\boldsymbol{H}_i^{\mathrm{T}} + \boldsymbol{R}_{i[k+1]} \tag{21}$$

When the speed estimation method fails, the state of the two adjacent time steps cannot satisfy Eq. (9), and the noise of $\boldsymbol{I}$ will no longer satisfy the zero mean Gaussian distribution, which will be manifested as colored noise. According to the χ^2 detection principle [38], the test statistics can be constructed as:

$$\lambda_{i[k]} = \boldsymbol{I}^{\mathrm{T}}_{i[k]}\left(\boldsymbol{H}_i\boldsymbol{P}^-_{i[k]}\boldsymbol{H}_i^{\mathrm{T}} + \boldsymbol{R}_{i[k]}\right)^{-1}\boldsymbol{I}_{i[k]} \tag{22}$$

During the acceleration and deceleration of magnetically suspended PMSM, the mean of $\boldsymbol{I}$ will slightly deviate from zero, leading to a slight increase in λ_i. On this basis, considering the probability of misdiagnosis, the threshold λ_t can be set. When λ_i of local Kalman filter KFi is greater than the fault detection threshold λ_t, it can be determined that the speed estimation method used as the measurement of KFi fails, and the abnormal speed information can be immediately isolated.

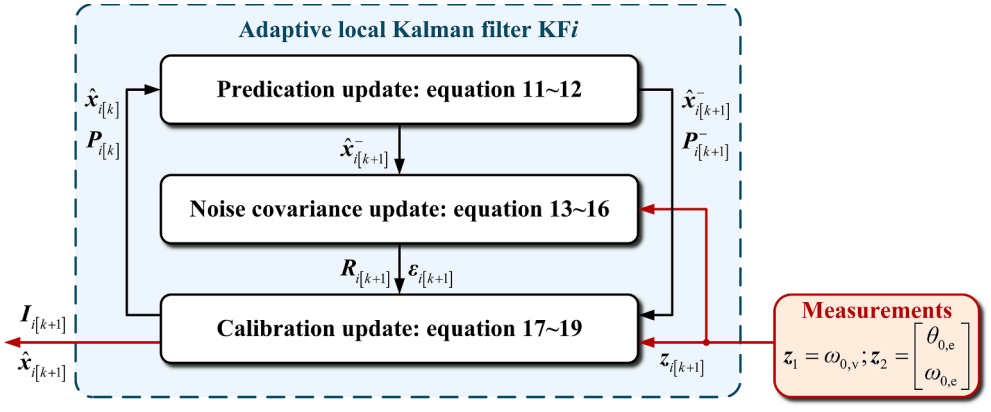

Fig. 6. Schematic diagram of the iterative process of the adaptive local Kalman filter.

4.3. Matrix weighted optimal fusion

In order to fully utilize the data advantage through two independent speed information, a further matrix weighted optimal fusion is also performed once obtaining the local state estimation $\widehat{\boldsymbol{x}}_i$ of KFi to obtain speed information with lower noise levels.

Firstly, composite error covariance is established based on the local state estimation error covariance of KFi:

$$\boldsymbol{P}_{[k]} = \begin{bmatrix} \boldsymbol{P}_{1[k]} & \boldsymbol{P}_{12[k]} \\ \boldsymbol{P}_{21[k]} & \boldsymbol{P}_{2[k]} \end{bmatrix} \tag{23}$$

Due to the independence of two speed information, the local state estimation error of KF1 and KF2 are uncorrelated, suggesting that the cross covariance $\boldsymbol{P}_{12} = \boldsymbol{P}_{21} = \boldsymbol{0}$.

Then, the fusion state estimation with matrix weights can be defined as:

$$\widehat{\boldsymbol{x}}_{\mathrm{f}[k]} = \boldsymbol{\Lambda}_{1[k]}\widehat{\boldsymbol{x}}_{1[k]} + \boldsymbol{\Lambda}_{2[k]}\widehat{\boldsymbol{x}}_{2[k]} \tag{24}$$

where:

$$\widehat{\boldsymbol{x}}_{\mathrm{f}} = \begin{bmatrix} \theta_{0,\mathrm{f}} \\ \omega_{0,\mathrm{f}} \end{bmatrix}$$

The error covariance of fusion state estimation is:

$$\boldsymbol{P}_{\mathrm{f}[k]} = \mathrm{E}\left[\left(\widehat{\boldsymbol{x}}_{\mathrm{f}[k]} - \boldsymbol{x}_{[k]} \right) \left(\widehat{\boldsymbol{x}}_{\mathrm{f}[k]} - \boldsymbol{x}_{[k]} \right)^{\mathrm{T}} \right] \tag{25}$$

When the trace of $\boldsymbol{P}_{\mathrm{f}[k]}$ meets a minimum value, it represents the lowest noise level of $\widehat{\boldsymbol{x}}_{\mathrm{f}}$. After solving, the expression for the optimal fusion matrix weights can obtained as follows:

$$\left[\boldsymbol{\Lambda}_{1[k]}, \boldsymbol{\Lambda}_{2[k]} \right] = \left(\boldsymbol{e}^{\mathrm{T}} \boldsymbol{P}_{[k]}^{-1} \boldsymbol{e} \right)^{-1} \boldsymbol{e}^{\mathrm{T}} \boldsymbol{P}_{[k]}^{-1} \tag{26}$$

where:

$$\boldsymbol{e} = \begin{bmatrix} 1 & 0 & 1 & 0 \\ 0 & 1 & 0 & 1 \end{bmatrix}^{\mathrm{T}}$$

After fusing $\widehat{\boldsymbol{x}}_1$ and $\widehat{\boldsymbol{x}}_2$ using $\boldsymbol{\Lambda}_1$ and $\boldsymbol{\Lambda}_2$, the error covariance of $\widehat{\boldsymbol{x}}_{\mathrm{f}}$ can be rewritten as:

$$\boldsymbol{P}_{\mathrm{f}[k]} = \left(\boldsymbol{e}^{\mathrm{T}} \boldsymbol{P}_{[k]}^{-1} \boldsymbol{e} \right)^{-1} \tag{27}$$

Considering the smaller trace of $\boldsymbol{P}_{\mathrm{f}[k]}$ as compared to those of $\boldsymbol{P}_{1[k]}$ and $\boldsymbol{P}_{2[k]}$, $\widehat{\boldsymbol{x}}_{\mathrm{f}}$ should possess a lower noise level as compared to the those of the two local state estimations $\widehat{\boldsymbol{x}}_1$ and $\widehat{\boldsymbol{x}}_2$. If $\omega_{0,\mathrm{v}}$ and $\omega_{0,\mathrm{e}}$ obtained by SOGI-FLL and FSMO-PLL are unbiased estimations of the true speed, the fused speed $\omega_{0,\mathrm{f}}$ will have higher estimation accuracy.

Combined with the research in section 4.1, the optimal fusion of speed information includes the following specific steps: Firstly, adaptive local Kalman filters KFi; $i = 1,2$ are adopted to obtain local state estimations of the two independent speed information, and the local state estimation error covariance $\boldsymbol{P}_i$ is obtained by iteration. Then, a composite error covariance $\boldsymbol{P}$ is constructed with the local state estimation error covariance. Based on the composite error covariance, the optimal fusion matrix weights $\boldsymbol{\Lambda}_i$ are solved, which decrease as the noise level in the speed information increases. At last, the matrix weights $\boldsymbol{\Lambda}_i$ are adopted to perform matrix weighted optimal fusion of the speed information, so as to obtain the fused speed $\omega_{0,\mathrm{f}}$ with higher estimation accuracy.

5. Experimental validations

5.1. Experimental test rig of magnetically suspended PMSM

In this paper, an experimental test rig was constructed with a magnetically suspended turbo molecular pump (MSTMP) with direct-drive structure. A dSPACE MicroLabBox-DS1202 was adopted to execute the control program of AMB, sensorless vector control program of PMSM and speed fault-tolerance and fusion strategy. DS1202 was connected to the host computer through an Ethernet interface, enabling real-time monitoring and collection of feedback signals, control signals and intermediate variables in control system. In the control system, the calculation frequency of AMB control system, the SVPWM switching frequency of the PMSM, the SOGI-FLL calculation frequency, the FSMO-PLL calculation frequency, and the calculation frequency of the SFTFS are all set to be 10 kHz. In terms of control hardware, a three-level half bridge power amplifier was used to drive the AMB, and a three-phase inverter bridge with IGBT module was used to drive the PMSM. The overall structure of the experimental test rig is shown in Fig. 7. The main parameters of the MSTMP used in the experiment are shown in Table 1, and the main parameters of the SFTFS are shown in Table 2.

5.2. Experimental validations of speed fault-tolerance ability

Firstly, SFTFS was activated to calculate the real-time fused speed, and MSTMP was accelerated to 12,000 r/min. In the control system of AMB, a generalized notch filter with notch angular frequency $\omega_{0,f}$ was introduced for unbalance compensation. The comparison of rotor displacement and control current before and after unbalance compensation is shown in Fig. 8(a) and Fig. 8(b), respectively. After activating the unbalance compensation, the vibration displacement of the rotor decreased from 23 μm to 10 μm, and the maximum control current also decreased from 0.477 A to 0.152 A, with a peak-to-peak value reduction of 82 %. The unbalance compensation effectively weakened the components with the same frequency of rotor speed in the control current and reduced the saturation risk of actuator for AMB.

The speed estimation curve under radial shock excitation is shown in Fig. 9(a). At 285.8 s, due to the shock excitation, the speed information obtained by SOGI-FLL failed and gradually decreased from 12,000 r/min to 0. However, $\omega_{0,e}$ was rarely affected and remained to be 12,000 r/min. According to the enlarged curve in Fig. 9(b), it can be seen that both speed estimation methods worked properly before the application of shock excitation and the SFTFS was capable of performing matrix weighted optimal fusion with $\omega_{0,v}$ and $\omega_{0,e}$. Once the $\omega_{0,v}$ failed, the SFTFS could diagnose and isolate the abnormal speed information within 5 ms, and the fluctuation of $\omega_{0,f}$ was within 2 r/min from the occurrence of fault to the completion of fault isolation. After completing the isolation of abnormal speed information, $\omega_{0,f}$ would become the local state estimation of $\omega_{0,e}$, ensuring the effectiveness of speed information. Owing to the stable value of $\omega_{0,f}$ around correct speed, the unbalance compensation was not affected by the shock excitation.

Fig. 10 gives the rotor vibration displacement under shock excitation. Obviously, no divergence phenomenon occurs. The displacement of the rotor only shows a slight overall deviation under shock excitation and quickly recovers to the normal position. If the speed information only provided by SOGI-FLL, the unbalance compensation will fail due to speed faults when subjected to shock excitation.

To simulate the scenario wherein the speed information obtained by FSMO-PLL fails, the MSTMP was reaccelerated to 12,000 r/min. At 287 s, all the three phase lines of the PMSM were disconnected simultaneously to simulate an unexpected power outage of the motor. As illustrated in Fig. 11(a), once the PMSM is powered off, the speed information obtained by FSMO-PLL fails and the rotor begins to naturally decelerate without driving. However, SOGI-FLL is not affected by the motor power outage and can still accurately estimate the speed during the deceleration process. Fig. 11(b) shows that when the PMSM is powered off, the SFTFS diagnoses and isolates abnormal speed information $\omega_{0,e}$. At this time, the fused speed $\omega_{0,f}$ becomes the local state estimation of $\omega_{0,v}$, ensuring the effectiveness of speed information. This indicates that when $\omega_{0,f}$ is used as the notch angular frequency of generalized notch filter, the unbalance compensation can operate properly during the deceleration process of the MSTMP.

Moreover, it can be seen that with the application of SFTFS, the vibration displacement of the rotor changes slightly and remains to be around 10 μm before and after the power outage of the motor (see Fig. 12). The experimental results mentioned above verify that the SFTFS can automatically diagnose and isolate abnormal speed information when one speed estimation method fails, significantly improving the reliability of the unbalance compensation.

5.3. Experimental validations of speed fusion ability

The harmonic components in the rotor vibration displacement would affect the speed estimation accuracy of SOGI-FLL, that is the noise level in $\omega_{0,f}$ would raise. To further validate the adaptive optimal fusion ability of SFTFS, speed information containing different noise levels were input into SFTFS, and the fused speed and the speed estimation error variance were analyzed. Specifically, to simulate the harmonic in rotor vibration displacement [39], the unbalance compensation was turned off to obtain the original total harmonic distortion (THD) of rotor vibration displacement, which is 6.68 %. Then, two sets of third harmonic disturbance with different amplitudes are introduced into the rotor vibration displacement, which causes the THD rises to 19.48 % and 33.25 % respectively. The

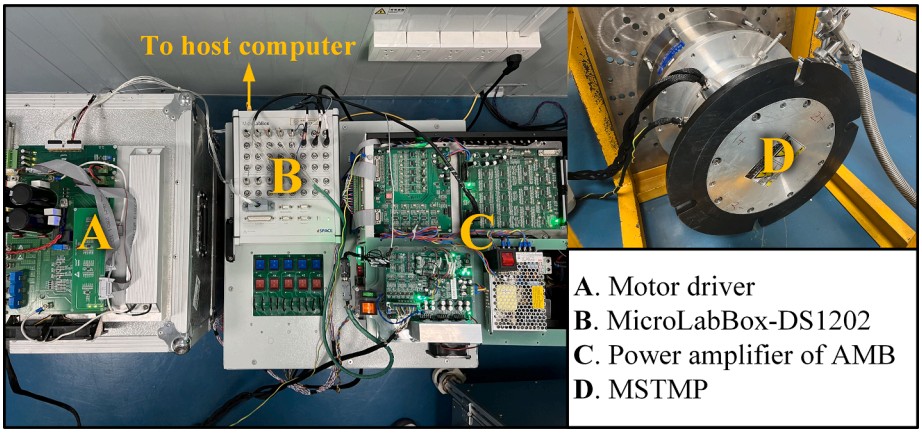

Fig. 7. The photo of experimental test rig.

Table 1
Main parameters of the MSTMP.

Parameters	Values
Mass of rotor	17.566 kg
Polar moment of inertia	0.0934 kg·m^2
Equatorial moment of inertia	0.1809 kg·m^2
Air gap of touchdown bearings	100 μm
Force/current factors of the AMBs at each end	898.75, 520.33
Force/displacement factors of the AMBs at each end	2.876×10^6, 1.665×10^6
Sampling time	0.0001 s
Rated speed of the PMSM	21,000 r/min
Rated power of the PMSM	3 kW
Stator resistance of the PMSM	300 mΩ
Stator inductance of the PMSM	1.29 mH
Pole pair of the PMSM	1

Table 2
Main parameters of SFTFS.

Parameters	Values
Frequency estimation gain of FLL γ	0.5
Current sliding mode gain of FSMO k_{i}	40
Back electromotive force sliding mode gain of FSMO k_{e}	220
Covariance matrix of system noise $\boldsymbol{Q}$	[0.001 0; 0 0.001]
Forgetting factor in noise update equations b	0.99
Fault diagnosis threshold λ_{t}	30

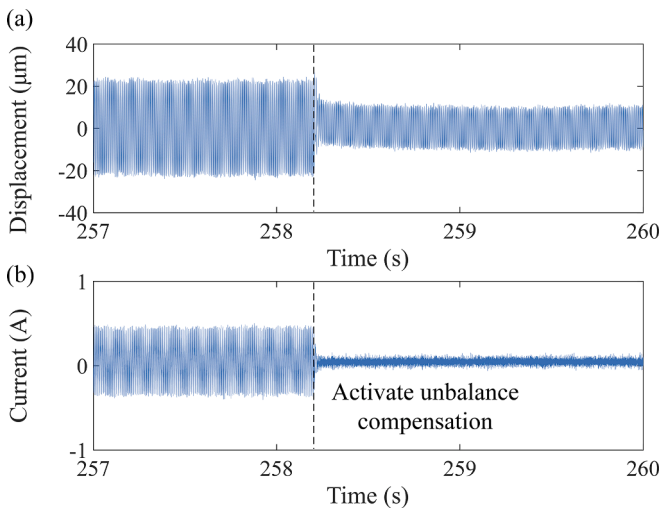

Fig. 8. Comparison diagram before and after unbalance compensation (a) Comparison diagram of rotor displacement (b) Comparison diagram of control current.

corresponding vibration displacement of rotor is presented in Fig. 13 (a). Then, the three types of rotor vibration displacements mentioned above (6.68 % THD, 19.48 % THD and 33.25 % THD) were employed as inputs for SOGI-FLL, and the corresponding $\omega_{0,\mathrm{v}}$, $\omega_{0,\mathrm{e}}$, and $\omega_{0,\mathrm{f}}$ are displayed in Fig. 13 (b). The speed estimation error variance $P_{\omega 1}$, $P_{\omega 2}$, and $P_{\omega \mathrm{f}}$ in $\boldsymbol{P}_1$, $\boldsymbol{P}_2$ and $\boldsymbol{P}_{\mathrm{f}}$ are given in Fig. 13 (c).

It is found that $P_{\omega 1}$ and $P_{\omega 2}$ corresponding to the local Kalman filter KF1 and KF2 are at similar level with 6.68 % THD, revealing that the noise level of speed term in the local state estimation $\widehat{\boldsymbol{x}}_1$ and $\widehat{\boldsymbol{x}}_2$ is similar. After matrix weighted optimal fusion, $P_{\omega \mathrm{f}}$ is smaller than $P_{\omega 1}$ and $P_{\omega 2}$, indicating that $\omega_{0,\mathrm{f}}$ has lower noise levels and higher speed estimation accuracy.

When the THD of rotor vibration displacement increases to 19.48 %, the peak-to-peak error of speed estimation in SOGI-FLL is about 7 r/min. Meanwhile, KF1 adaptively adjusts the measurement noise covariance based on the noise level of $\omega_{0,\mathrm{v}}$, and the iterated $P_{\omega 1}$ also increases to 0.002. However, the harmonic in the rotor vibration displacement rarely affects FSMO-PLL, and $P_{\omega 2}$ remains to be unchanged and much smaller than $P_{\omega 1}$. Therefore, in the process of matrix weighted optimal fusion, $\widehat{\boldsymbol{x}}_2$ has a greater weight than $\widehat{\boldsymbol{x}}_1$, and $P_{\omega \mathrm{f}}$ is closer to $P_{\omega 2}$ while slightly smaller than $P_{\omega 2}$.

When the THD of rotor vibration displacement increases to 33.25 %, the noise component in $\omega_{0,\mathrm{v}}$ further increases and the peak-to-

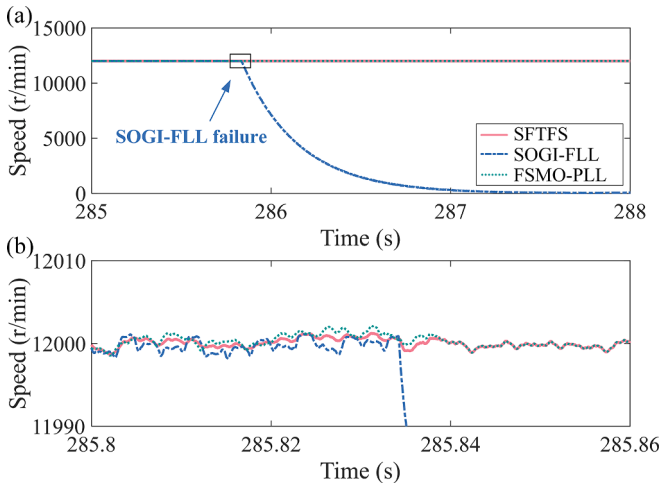

Fig. 9. Speed estimation curve under shock excitation (a) Overall speed variation trend (b) Details of speed curve during the time period of 285.8 s to 285.86 s.

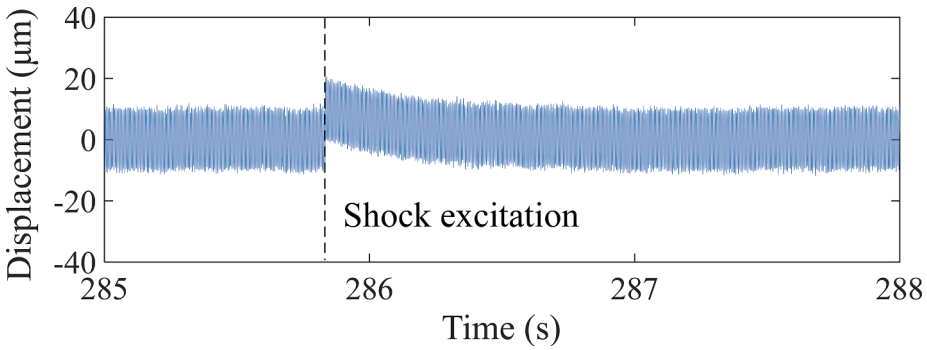

Fig. 10. Rotor vibration displacement under shock excitation.

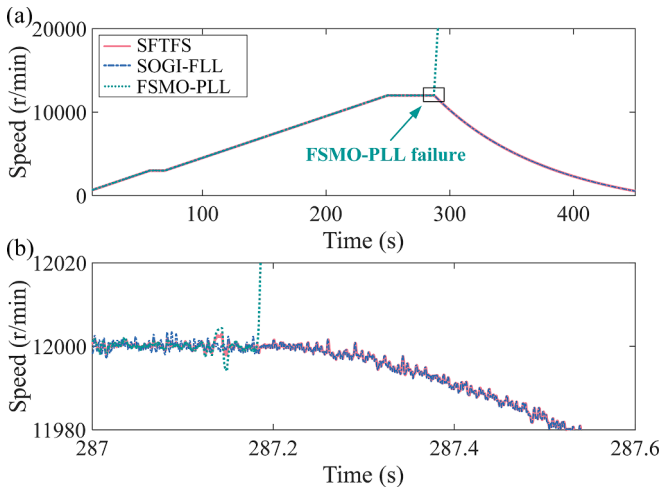

Fig. 11. Speed estimation curve under motor power outage (a) Overall speed variation trend (b) Details of speed curve during the time period of 287 s to 287.6 s.

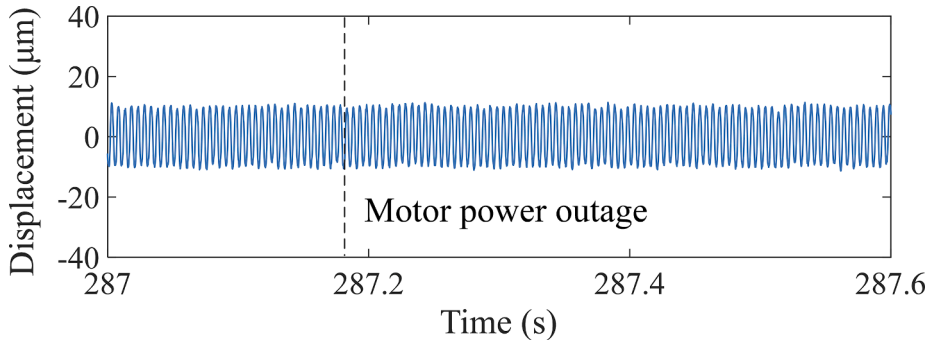

Fig. 12. Rotor vibration displacement under motor power outage.

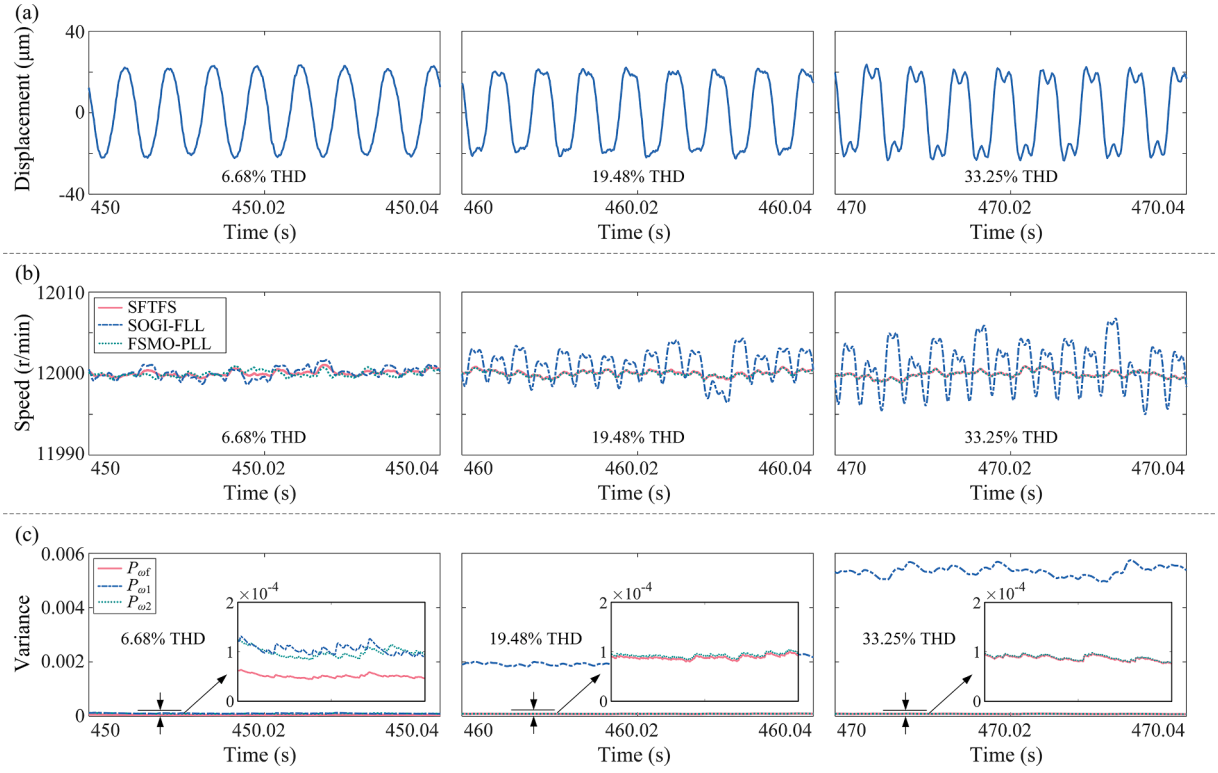

Fig. 13. Experimental results of speed fusion under harmonic disturbance (a) Rotor vibration displacement (b) Speed estimation curve (c) Speed estimation error variance.

peak value of speed estimation error rises to 12 r/min. $P_{\omega 1}$ also increases to 0.0055, further enhancing the weight of $\hat{\boldsymbol{x}}_2$ in the process of matrix weighted optimal fusion, while the weight of $\hat{\boldsymbol{x}}_1$ with higher noise content would further decrease. Finally, the fused speed $\omega_{0,\mathrm{f}}$ almost coincides with $\omega_{0,\mathrm{e}}$, and $P_{\omega \mathrm{f}}$ is similar to $P_{\omega 2}$.

The results demonstrate that the SFTFS can perform adaptive optimal fusion of $\omega_{0,\mathrm{v}}$ and $\omega_{0,\mathrm{e}}$ based on the noise level of speed information provided by SOGI-FLL and FSMO-PLL. The fused speed $\omega_{0,\mathrm{f}}$ with a smaller error variance can be consequently obtained, which reduces the noise level of speed estimation and improves the accuracy of speed estimation.

6. Conclusion

A speed fault-tolerance and fusion strategy is proposed to develop high-reliability rotor speed estimation method for implementing unbalance compensation of magnetically suspended PMSM. The newly-developed strategy, which involving in the acquisition of two independent yet redundant speed information from the rotor vibration displacement and electrical signals, makes it feasible to yield automatic diagnosis and isolation of abnormal speed information when one speed estimation method fails. Additionally, when both

speed estimation methods are functioning normally, the strategy performs real-time adaptive optimal fusion to strengthen the accuracy of speed information. The applicability of strategy was experimentally validated on a MSTMP, revealing its effectiveness and superiority.

It is also worth noting that the acquisition of speed information is not restricted to be using SOGI-FLL and FSMO-PLL. If more speed estimation methods are applied or required, one can enlarge the numbers of local Kalman filter to enhance the fault-tolerance and fusion capability and thus increasing the reliability as well as precision of speed information. More importantly, the fused speed information can also be potentially applied to other control methods of AMB requiring speed information, i.e., gyroscopic effect suppression and harmonic currents suppression.

CRediT authorship contribution statement

Runhui Yao: Writing – original draft, Visualization, Methodology, Investigation, Data curation, Conceptualization. **Yuanping Xu:** Writing – review & editing, Supervision. **Renkun Zhang:** Writing – original draft, Validation, Formal analysis. **Yue Zhang:** Writing – review & editing, Supervision. **Jin Zhou:** Writing – review & editing, Supervision, Funding acquisition.

Declaration of competing interest

The authors declare that they have no known competing financial interests or personal relationships that could have appeared to influence the work reported in this paper.

Data availability

Data will be made available on request.

References

[1] X. Xu, Q. Han, A general electromagnetic model and vibration control for shape deviations in PMSM supported by three-pole active magnetic bearings, Mech. Syst. Sig. Process. 158 (2021) 107710.
[2] Q. Zhang, L. Tan, G. Xu, Evaluating transient performance of servo mechanisms by analysing stator current of PMSM, Mech. Syst. Sig. Process. 101 (2018) 535–548.
[3] Y. Yao, H. Sha, Y. Su, G. Ren, S. Yu, Identification of system parameters and external forces in AMB-supported PMSM system, Mech. Syst. Sig. Process. 166 (2022) 108438.
[4] S. Zheng, J. Yang, X. Song, C. Ma, Tracking compensation control for nutation mode of high-speed rotors with strong gyroscopic effects, IEEE Trans. Ind. Electron. 65 (2018) 4156–4165.
[5] B. Han, Y. Chen, S. Zheng, M. Li, J. Xie, Whirl mode suppression for AMB-rotor systems in control moment gyros considering significant gyroscopic effects, IEEE Trans. Ind. Electron. 68 (2021) 4249–4258.
[6] K. Wang, Q. Zhong, K. Mao, S. Zheng, B. Chen, B. Dong, Rotor temperature estimation for magnetically suspended turbo molecular pump based on flux linkage identification, IEEE/ASME Trans. Mechatron. 27 (2022) 5780–5791.
[7] B. Han, K. Xiong, K. Mao, Estimation of temperature in turbo-molecular pump based on motor resistance online identification, Vacuum 169 (2019) 108935.
[8] B. Xiang, Z. Li, W. Wong, Stiffness identification of magnetic suspension system based on zero-displacement and zero-current models, Mech. Syst. Sig. Process. 171 (2022) 108901.
[9] B. Xiang, X. Wang, W. Wong, Process control of charging and discharging of magnetically suspended flywheel energy storage system, J. Storage Mater. 47 (2022) 103629.
[10] R. Tiwari, P. Kumar, An innovative virtual trial misalignment approach for identification of unbalance, sensor and active magnetic bearing misalignment along with its stiffness parameters in a magnetically levitated flexible rotor system, Mech. Syst. Sig. Process. 167 (2022) 108540.
[11] Mechanical vibration — Vibration of rotating machinery equipped with active magnetic bearings – Part 4: Technical guidelines, ISO Standard 14839-4 (2012).
[12] P. Cui, Y. Li, J. Li, L. Du, Y. Wu, Synchronous vibration force suppression of magnetically suspended CMG based on modified double SOGI-FLL, IEEE Trans. Ind. Electron. 70 (2023) 11566–11575.
[13] Q. Zhang, T. Jiang, X. Wei, Instantaneous speed estimation of induction motor by time-varying sinusoidal mode extraction from stator current, Mech. Syst. Sig. Process. 200 (2023) 110608.
[14] C. Peng, J. He, M. Zhu, Z. Deng, Z. Zhen, Q. Liu, Optimal synchronous vibration control for magnetically suspended centrifugal compressor, Mech. Syst. Sig. Process. 132 (2019) 776–789.
[15] Q. Chen, G. Liu, B. Han, Suppression of imbalance vibration in AMB-rotor systems using adaptive frequency estimator, IEEE Trans. Ind. Electron. 62 (2015) 7696–7705.
[16] P. Cui, L. Du, X. Zhou, J. Li, Y. Li, Y. Wu, Synchronous vibration moment suppression for AMBs rotor system in control moment gyros considering rotor dynamic unbalance, IEEE/ASME Trans. Mechatron. 27 (2022) 3210–3218.
[17] X. Guan, J. Zhou, C. Jin, H. Wu, Y. Lin, Adaptive surge detection of magnetic suspension centrifugal blower based on rotor radial displacement signal and SOGI-FLL with prefilter, Meas. Sci. Technol. 33 (2022) 065304.
[18] X. Guan, J. Zhou, C. Jin, Y. Lin, Surge detection of magnetic suspension fluid machinery based on rotor axial displacement signal and normalized second-order generalized integrator-frequency locked loop with prefilter, J. Vib. Control 29 (2023) 4935–4947.
[19] Y. Zhang, J. Zhou, X. Han, Y. Zhou, Adaptive odd repetitive control for magnetically suspended rotor harmonic currents suppression, J. Vib. Control 29 (2023) 2077–2085.
[20] R. Yang, W. Pei, Y. Yang, Z. Deng, C. Peng, A novel method for rotational speed observation of magnetically suspended high speed motor using quadrature phase-locked-loop, IEEE Sens. J. 22 (2022) 8604–8613.
[21] H. Xu, J. Li, K. Yang, Y. Lu, P. Zhang, Vibration suppression of active magnetic bearing system with precise frequency estimation method, in: 2022 International Conference on Electrical Machines (ICEM), IEEE, Valencia, Spain, 2022, pp. 171–177.
[22] J. Li, Q. Wang, L. Xiao, Z. Liu, Q. Wu, An accurate and robust adaptive notch filter-based phase-locked loop, J. Power Electron. 20 (2020) 1514–1525.
[23] B. Liu, M. An, H. Wang, Y. Chen, Z. Zhang, C. Xu, S. Song, Z. Lv, A Simple Approach to Reject DC Offset for Single-Phase Synchronous Reference Frame PLL in Grid-Tied Converters, IEEE Access 8 (2020) 112297–112308.
[24] H. Zheng, Z. Liu, R. An, J. Liu, K. Feng, Y. Tu, Discrete multiple second-order generalized integrator with low-pass filters and frequency-locked loop for DC rejection, IEEE Trans. Power Electron. 37 (2022) 11814–11827.

[25] P. Rodriguez, A. Luna, I. Candela, R. Mujal, R. Teodorescu, F. Blaabjerg, Multiresonant frequency-locked loop for grid synchronization of power converters under distorted grid conditions, IEEE Trans. Ind. Electron. 58 (2011) 127–138.
[26] M. Hutterer, G. Kalteis, M. Schrödl, Redundant unbalance compensation of an active magnetic bearing system, Mech. Syst. Sig. Process. 94 (2017) 267–278.
[27] S. Qiao, Y. Fan, G. Wang, H. Zhang, A modified federated Student's t-based variational adaptive Kalman filter for multi-sensor information fusion, Measurement 222 (2023) 113577.
[28] Z. Xing, Y. Xia, Distributed Federated kalman filter fusion over multi-sensor unreliable networked systems, IEEE Trans. Circuits Syst. I (63) (2016) 1714–1725.
[29] Z. Wang, N. Li, Z. Wang, F. Zhu, X. Du, An adaptive federated filter based on variational bayes with application to multisource navigation, IEEE Sens. J. 23 (2023) 9859–9870.
[30] H. Xiong, Z. Mai, J. Tang, F. He, Robust GPS/INS/DVL navigation and positioning method using adaptive federated strong tracking filter based on weighted least square principle, IEEE Access 7 (2019) 26168–26178.
[31] L. Gao, X. Xia, Z. Zheng, J. Ma, GNSS/IMU/LiDAR fusion for vehicle localization in urban driving environments within a consensus framework, Mech. Syst. Sig. Process. 205 (2023) 110862.
[32] Z. Yin, Y. Zhang, X. Cao, D. Yuan, J. Liu, Estimated position error suppression using novel PLL for IPMSM sensorless drives based on full-order SMO, IEEE Trans. Power Electron. 37 (2022) 4463–4474.
[33] L. Yuan, K. Han, C. Zhang, X. Zhu, Y. Ding, Comparative analysis of full-order SMO and STM-MRAS in SPMSM sensorless drive system, IEEE J. Emerg. Sel. Topics Power Electron. 12 (2024) 2592–2603.
[34] S. Sun, H. Cheng, W. Wang, H. Liu, S. Mi, X. Zhou, Sensorless DPCC of PMLSM Using SOGI-PLL Based High-Order SMO with Cogging Force Feedforward Compensation, in: 2021 13th International Symposium on Linear Drives for Industry Applications (LDIA), IEEE, Wuhan, China, 2021, pp. 1–7.
[35] M. Song, R. Astroza, H. Ebrahimian, B. Moaveni, C. Papadimitriou, Adaptive Kalman filters for nonlinear finite element model updating, Mech. Syst. Sig. Process. 143 (2020) 106837.
[36] K. Yuen, Y. Liu, W. Yan, Estimation of time-varying noise parameters for unscented Kalman filter, Mech. Syst. Sig. Process. 180 (2022) 109439.
[37] C. Zhu, S. Wang, C. Yu, H. Zhou, C. Fernandez, J.M. Guerrero, An improved Cauchy robust correction-sage Husa extended Kalman filtering algorithm for high-precision SOC estimation of Lithium-ion batteries in new energy vehicles, J. Storage Mater. 88 (2024) 111552.
[38] Y. Wang, N. Masoud, A. Khojandi, Real-time sensor anomaly detection and recovery in connected automated vehicle sensors, IEEE Trans. Intell. Transport. Syst. 22 (2021) 1411–1421.
[39] K. Cai, Z. Deng, C. Peng, K. Li, Suppression of harmonic vibration in magnetically suspended centrifugal compressor using zero-phase odd-harmonic repetitive controller, IEEE Trans. Ind. Electron. 67 (2020) 7789–7797.